ADVANCED MATERIALS INTERFACES
www.advmatinterfaces.de

# Growth Dynamics of Millimeter-Sized Single-Crystal Hexagonal Boron Nitride Monolayers on Secondary Recrystallized Ni (100) Substrates

*Hao Tian, Yanwei He, Protik Das, Zhenjun Cui, Wenhao Shi, Alireza Khanaki, Roger K. Lake, and Jianlin Liu**

**The outstanding physical properties of 2D materials have sparked continuous research interest in exploiting these materials for next-generation high-performance electronic and photonic technology. Scalable synthesis of high-quality large-area 2D hexagonal boron nitride (h-BN) is a crucial step toward the ultimate success of many of these applications. In this work, a synthetic approach in which secondary recrystallized Ni (100) substrates underwent a carburization process, followed by the growth of h-BN in a molecular beam epitaxy system is designed. The h-BN growth dynamics is studied by tuning different growth parameters including the substrate temperature, and the boron and nitrogen source flux ratio. With assistance from density functional theory calculations, the role of interstitial C atoms in promoting h-BN growth by enhancing the catalytic effect of the transition metal, which lowers the nucleation activation energy barrier, is rationalized. Through the control of the growth parameters, a single-crystal h-BN monolayer domain as large as 1.4 mm in edge length is achieved. In addition, a high-quality, continuous, large-area h-BN single-layer film with a breakdown electric field of 9.75 MV cm$^{-1}$ is demonstrated. The high value of the breakdown electric field suggests that single-layer h-BN has extraordinary dielectric strength for high-performance 2D electronics applications.**

## 1. Introduction

Within the 2D material family, hexagonal boron nitride (h-BN) plays a critical role as the 2D dielectric and wide bandgap semiconductor.[1–4] In recent years, there have been many reports on large-area single-crystal graphene and transition metal dichalcogenides (TMDs) well over a few millimeter to centimeter[5,6] as well as a variety of industrially scalable approaches.[7,8] In comparison, the development of the 2D h-BN is relatively immature. The domain size is mostly less than 100 µm. Reports on h-BN domains with a size close to 1 mm are rare.[9,10] Although wafer-scale single crystals have been reported through the coalescence of identically aligned h-BN domains,[11] on twin-free single-crystal Rh (111) thin films,[12] and on low-symmetry Cu (110) vicinal surface,[13] it is noted that discrete h-BN domains or flakes over 1 mm have not been reported, and the understanding of the growth dynamics remains elusive. Controllable synthesis of large-size single-crystal h-BN is highly desirable but challenging. A great deal of h-BN synthesis is carried out on various transition metal substrates, such as Cu,[1,2,14] Co,[15,16] Ni,[17,18] and Fe,[19–21] thanks to their catalytic activities favorable for the nucleation and growth of high-quality h-BN. Nevertheless, rational engineering of catalytic effects of a given transition metal substrate by alloying or incorporating dissimilar species has been rarely studied for the h-BN growth in order to enhance the control of layer number, nucleation density, and domain size; the only available efforts to date are Si-doping or N-doping of Fe substrates,[19,21] oxygen passivation of Cu substrates,[22] and carbon incorporation of Co/Ni substrates.[10]

While majority of the h-BN synthesis effort have been performed using chemical vapor deposition (CVD), molecular beam epitaxy (MBE) is versatile in terms of its ability to precisely control solid, gas, and plasma sources and tune the growth parameters. MBE has already been used to grow 2D h-BN and h-BN/graphene heterostructures.[10,23–29] In this work, we report the synthesis of millimeter-size single-crystal h-BN domains through an interstitial carbon assisted approach in an MBE system. While the interstitial carbon assisted growth of h-BN has been proposed in our recent effort,[10] leading to a large single-crystal h-BN flake of 600–700 µm, it is essential to achieve even larger single-crystal h-BN flakes with edge lengths on the order of millimeters or even continuous wafer-scale single-crystal 2D films. In addition, the growth thermodynamics and kinetics in terms of temperature-dependent growth and substrate surface engineering have not been comprehensively studied; numerical simulations are necessary to further elucidate the effect of the carbon incorporation on the

H. Tian, Y. He, Dr. P. Das, Z. Cui, W. Shi, Dr. A. Khanaki, Prof. R. K. Lake, Prof. J. Liu
Department of Electrical and Computer Engineering
University of California
Riverside, CA 92521, USA
E-mail: jianlin@ece.ucr.edu

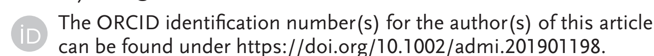
The ORCID identification number(s) for the author(s) of this article can be found under https://doi.org/10.1002/admi.201901198.

DOI: 10.1002/admi.201901198

 © 2019 WILEY-VCH Verlag GmbH & Co. KGaA, Weinheim

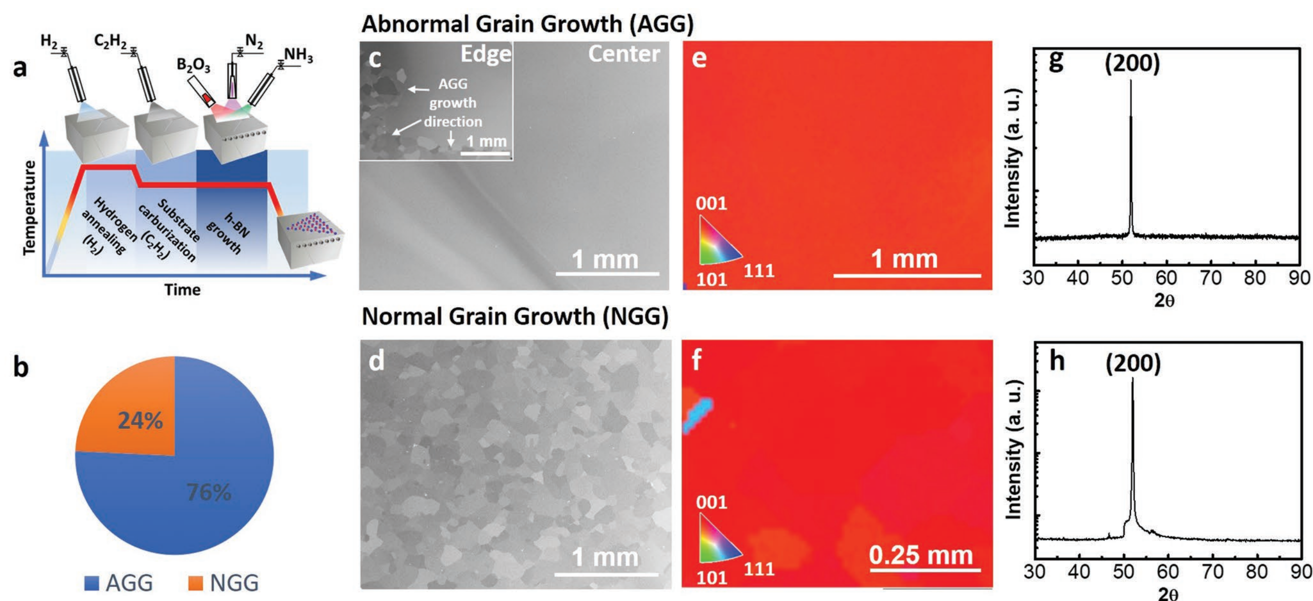


**Figure 1.** Characterization of Ni substrate after annealing. a) Schematic of a typical growth procedure. b) Statistics of 100 AGG and NGG samples with annealing temperature at 950 °C and growth temperature from 890 to 950 °C. c,d) SEM images, e,f) EBSD mapping, and g,h) XRD spectra of postannealed AGG and NGG Ni substrates, respectively. Inset in (c) shows an SEM image at the edge of the sample where boundary between AGG and NGG can be clearly seen. The white arrows indicate the migration directions of the abnormal grain.

tuning of the catalytic activities of transition metal substrates for complete controlled growth of large 2D h-BN single crystals. Here, we designed Ni substrates with carburization process through pretreatment of secondary recrystallized Ni with acetylene prior to the actual growth of h-BN. The growth dynamics were studied by tuning different growth parameters including substrate temperature, and B and N source ratio. From the perspective of activation energy through density functional theory (DFT) calculations, we rationalized the role of interstitial carbon incorporation in enhancing the catalytic activities of the transition metals. Through the control of the growth parameters, a single-crystal h-BN monolayer domain with a size as large as 1.4 mm in edge length was achieved. Furthermore, a high-quality continuous single-layer h-BN with a high breakdown electric field of 9.75 MV $cm^{-1}$ was demonstrated.

## 2. Results and Discussion

We adopt a simple MBE growth procedure as illustrated in **Figure 1**a, in which Ni substrate undergoes three growth steps including hydrogen annealing, substrate carburization, and h-BN growth (Experimental Section). The hydrogen annealing temperature is controlled at 950 °C, which is slightly higher than the growth temperature (890–950 °C), in order to enhance the recrystallization of Ni. Figure 1b–h summarizes morphology results of Ni substrates after 1 h hydrogen annealing at 950 °C. The grains in as-received Ni foils have been deformed by cold rolling, and, as a result, additional dislocations are formed, and the grain boundary surface area is increased. Upon annealing, recrystallization and grain growth occur in order to reduce the internal energy. In general, there are two different types of grain growth, which are normal grain growth (NGG) and abnormal grain growth (AGG).[30] NGG usually stops when the average grain size is comparable with the substrate thickness, and the grain size is uniformly distributed. AGG is also known as secondary recrystallization, in which only a small population of the grains which are favored will grow in consumption of another population which is not favored, due to the surface and interface energy anisotropy, resulting in the formation of considerably large grains.[30] Figure 1c shows a scanning electron microscope (SEM) image of a typical Ni substrate with AGG grains (denoted as AGG Ni) after 1 h hydrogen annealing at 950 °C . The majority of the substrate consists of only a few grains with a size of a few millimeters. The inset image was taken at the edge of the sample where the boundary between AGG grains and NGG grains is identified. The AGG growth direction is indicated by the white arrows. In contrast, typical NGG Ni with the same annealing condition has small grains with an average size of ≈100 µm, which is comparable to the foil thickness. Electron backscatter diffraction (EBSD) mapping reveals that the dominant texture is (100) for both AGG and NGG Ni (Figure 1e,f), which is also confirmed by X-ray diffraction (XRD) as seen in Figure 1g,h, respectively. This is because (100) grains have lower strain energy density compared to grains with other surface planes in the elastic region.[31] The narrow peak in XRD in Figure 1g reveals good single crystallinity for the AGG substrate compared to wider peak in Figure 1h for NGG Ni. Even though majority of the substrates used in this work have gone through AGG, a small portion of them shows only NGG. Statistics of 100 samples grown at 890–950 °C after 1 h annealing at 950 °C shows that AGG occurance is 76%, while NGG occurs in the remaining 24%. We attribute this to the variation in strain and stress level during the cold working process in the as-received Ni foils. In

 © 2019 WILEY-VCH Verlag GmbH & Co. KGaA, Weinheim

**Table 1.** Summary of growth conditions of the typical samples.

| Step | Parameters | Sample I | Sample II | Sample III | Sample IV |
|---|---|---|---|---|---|
| Hydrogen annealing | Substrate | Ni (AGG) | Ni (AGG) | Ni (NGG) | Ni (AGG) |
| | Substrate temperature [°C] | 950 | 950 | 950 | 950 |
| | Hydrogen gas flow [sccm] | 10 | 10 | 10 | 10 |
| | Duration [min] | 60 | 60 | 60 | 60 |
| Carburization | Acetylene gas flow [sccm] | 0.5 | 0.5 | 0.5 | 0.5 |
| | Duration [s] | 300 | 300 | 300 | 300 |
| | Substrate temperature [°C] | 910 | 910 | 910 | 910 |
| h-BN growth | Substrate temperature [°C] | 910 | 910 | 910 | 910 |
| | Boron cell temperature [°C] | 1150 | 1120 | 1120 | 1130 |
| | Ammonia gas flow [sccm] | 5 | 10 | 10 | 10 |
| | Nitrogen gas flow [sccm] | 10 | 0 | 0 | 0 |
| | Nitrogen ECR current [mA] | 60 | – | – | – |
| | Duration [h] | 8 | 8 | 8 | 8 |

general, secondary recrystallization is a cheap and easy way to produce single-crystal metal. Different methods such as cyclic heat treatment and impurity incorporation have been reported to enhance the AGG.[32,33] The engineering of postprocessing procedure in order to produce AGG is beyond the scope of this work. Here, we focus on the study of h-BN growth on AGG Ni (100) substrates.

The next crucial step for enabling the formation and growth of h-BN including large single-crystal flakes and high-quality continuous films is the incorporation of carbon in these Ni (100) substrates. **Table 1** summarizes four typical h-BN samples (Samples I–IV), and all these samples underwent a carburization process by introducing a 0.5 sccm acetylene flux for 300 s at 910 °C. **Figure 2**a shows an SEM image of a reference sample grown with the same growth condition as Sample II except that there was no substrate carburization step. As seen from the image, the sample shows typical AGG Ni grains and texture without any h-BN on the substrate. Figure 2b shows the statistical summary of 58 samples regarding the effect of substrate carburization on the h-BN growth on AGG Ni (100) at different temperature. Without carburization, the growth of h-BN was not successful, as indicated by the red markers at zero carburization time in the figure. With carburization, there is a temperature window for successful h-BN growth as indicated by blue dashed lines in the figure. In addition, the growth temperature window opens up wider as the carburization time increases. As the growth temperature is lower than ≈875 °C, only some sparse white features, which are not h-BN, were deposited on the substrates, as shown in Figure S1 (Supporting Information). This region lies in kinetically controlled region due to low-temperature effect[34,35] and is labeled as reaction-limited region. As the growth temperature is higher than ≈960–980 °C indicated by the right blue dashed line in the figure, no h-BN could be grown due to high desorption of B and N atoms. It should be noted that the amount of carbon dissolved in the Ni substrates during the carburization process here is low, thus they will not precipitate to be incorporated into h-BN film or form graphene during the sample cooling period.

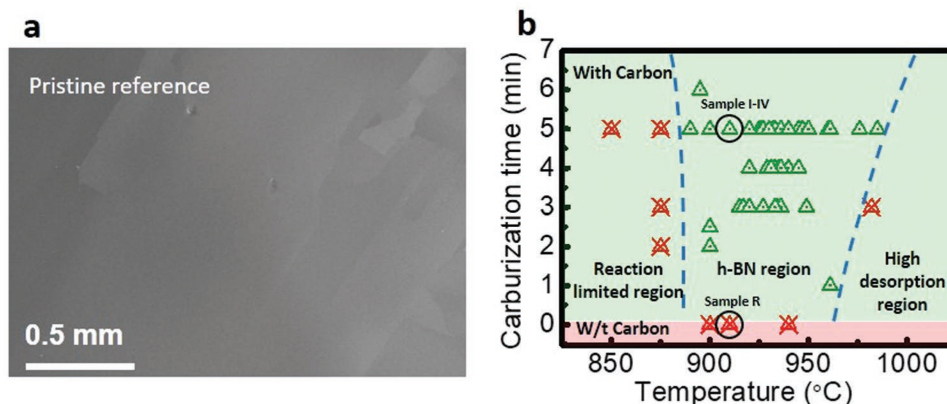


**Figure 2.** a) SEM image of a reference sample grown with the same growth condition as Sample II except the substrate carburization step. b) Summary of 58 samples grown at different carburization time and substrate temperature. Green marks label successful h-BN growth, and red marks label unsuccessful h-BN growth. The h-BN growth duration for green-marked samples is between 3 and 8 h, while the growth of red-marked samples lasted more than 6 h. The blue dashed lines are guide of eyes to identify the h-BN growth window. The circles indicate where the reference sample in (a) and Samples I–IV described in Table 1 are located.


© 2019 WILEY-VCH Verlag GmbH & Co. KGaA, Weinheim

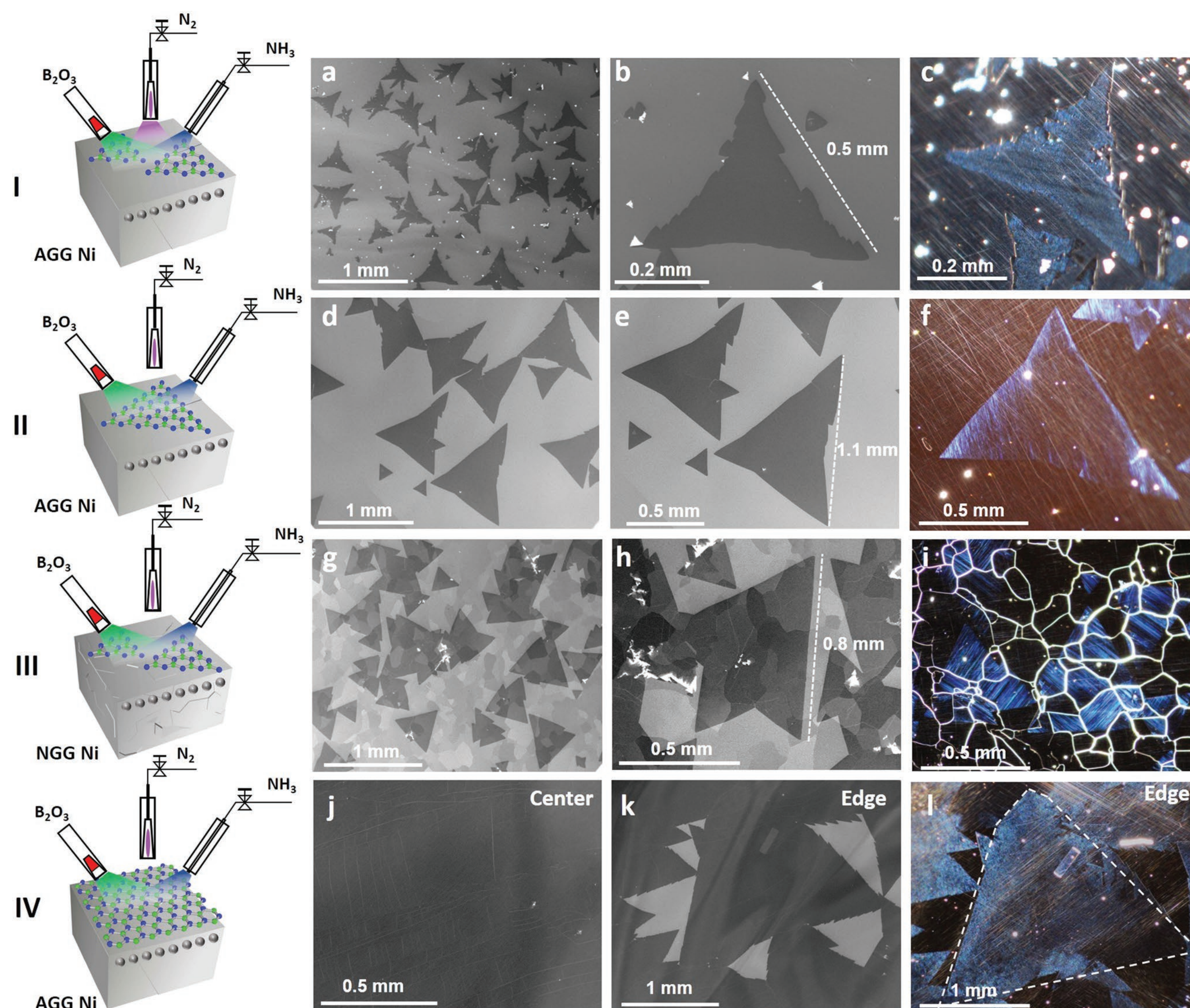


**Figure 3.** Overview of mm-sized single-crystal h-BN flakes and continuous h-BN monolayer. Large-area SEM, small-area SEM, DF-OM images of single-crystal h-BN flakes grown with a–c) a mixture of 10 sccm $N_2$ plasma and 5 sccm $NH_3$ on AGG Ni (Sample I), d–f) 10 sccm $NH_3$ on AGG Ni (Sample II), and g–i) 10 sccm $NH_3$ on NGG Ni (Sample III). j) SEM image of the center area, and k,l) SEM and DF-OM images of the edge area, respectively, of a continuous h-BN monolayer sample grown on AGG Ni with 10 sccm $NH_3$ and $B_2O_3$ effusion cell temperature at 1130 °C (Sample IV). Detailed growth conditions of these samples are summarized in the Table 1.

Detailed experimental proof can be found elsewhere.[10,29] The rationale of the carburization effect on the growth of h-BN can be further clarified as we continue to discuss the experiment and simulation details.

**Figure 3** gives an overview of h-BN growth under typical conditions (Samples I–IV). Sample I was grown using a mixture of nitrogen plasma and ammonia ($NH_3$) as the nitrogen source (refered as mixed nitrogen source). Sample I serves as the baseline sample as similar growth condition was reported in the previous work.[10] Nitrogen plasma can provide N radicals. On the other hand, $NH_3$ can be efficiently decomposed to absorbed N atoms on hot Ni surface, for example, at a temperature of 430 K, a decomposition efficiency of 23% was attained.[36] While the mixture of nitrogen plasma and ammonia gas can potentially provide more N sources, the chemistry of the formation of h-BN can be more complicated compared with sole nitrogen sources. Here, pure $NH_3$ gas was adopted as the N source in the growth of Samples II–IV. Figure 3a–c shows SEM and dark-field optical microscope (DF-OM) images of Sample I. Complementary to SEM imaging, DF-OM imaging is also a nondestructive method to effectively visualize 2D material on metal.[37] DF-OM imaging relying on scattered light can pick up the uneveness on a surface easily. As seen from Figure 3a–c, h-BN flakes over 0.5 mm were achieved. Figure 3d–f shows SEM and DF-OM images of Sample II. H-BN flakes with a size over 1 mm were achieved with lower nucleation density compared to Sample I. Sample III was grown under the same condition with Sample II. However, Ni substrate in Sample II underwent AGG, thus it can be treated as single-crystal substrate, while only NGG was observed in Sample III. In comparison to Sample II, both flake

 © 2019 WILEY-VCH Verlag GmbH & Co. KGaA, Weinheim

size and uniformity were compromised (Figure 3g–i). h-BN adlayers (white features) can be occasionally observed across the sample. As discussed above, even though both AGG and NGG Ni substrates are uniform in texture with (100) as the dominant texture, more grain boundaries on NGG substrate act as additional preferential nucleation sites for h-BN. Increased roughness also hinders the surface diffusion of adatoms which limits the domain size. Growth condition was further controlled by increasing B source flux. As the B cell temperature increases to 1130 °C, continuous h-BN film (Sample IV) was achieved on AGG Ni as seen in Figure 3j–l. Figure 3j shows an SEM image of the center of the sample where continuous h-BN film is observed. Figure 3k,l show an SEM image and a DF-OM image of the edge area of the sample, respectively. By comparing the SEM and DF-OM imaging at the same area, a flake with a size close to 2 mm can be identified using the contrast in DF-OM (Figure 3l). The grain boundary is revealed under DF-OM because the thermal induced corrugation depends on the alignment between h-BN and the metal substrate.[38]

X-ray photoemission spectroscopy (XPS) was performed on as-grown Sample II to further confirm the existence and stoichiometry of h-BN. The binding energies of B 1s and N 1s are shown to be at 190.0 and 397.5 eV, respectively (**Figure 4**a), with a stoichiometry ratio of unity. The sample was further transferred onto a variety of substrates for further characterizations. Figure 4b shows a UV–vis absorption spectrum performed after the sample was transferred onto a sapphire substrate. A strong peak at 203 nm with a sharp absorption edge can be observed, corresponding to a bandgap of 6.02 eV for h-BN extracted from the Tauc equation for a direct bandgap (inset in Figure 4b).[39] Figure 4c shows an OM image of the h-BN flakes transferred onto a $SiO_2$/Si substrate. Raman spectroscopy was further performed on the transferred sample. An $E_{2g}$ phonon mode at 1371 $cm^{-1}$ can be found in the Raman spectrum with

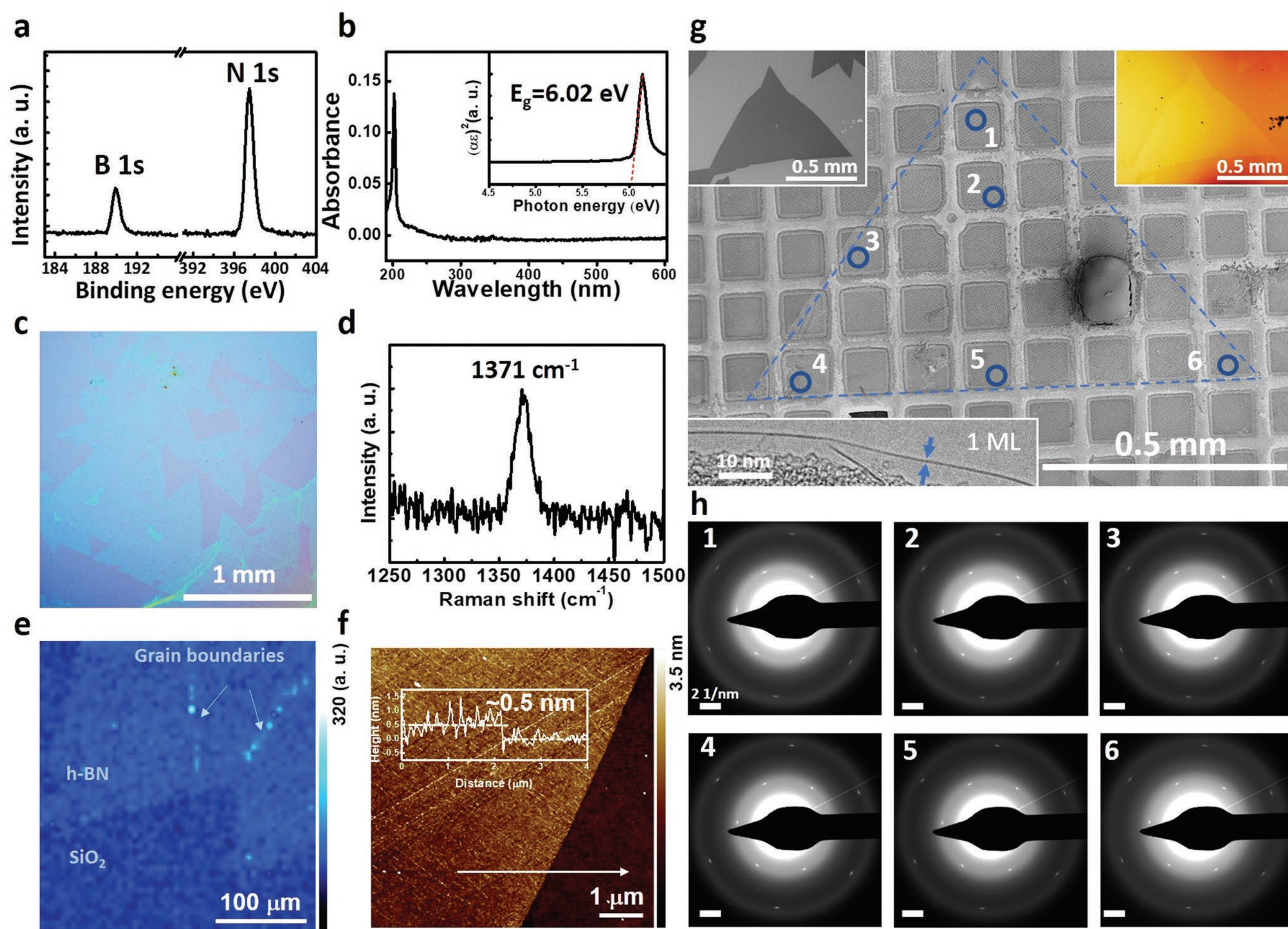


**Figure 4.** Characterization of typical single h-BN flake (Sample II). a) XPS B 1s and N 1s spectra. b) UV–vis absorption spectrum of a transferred h-BN sample on sapphire. Inset is $(A\varepsilon)^{1/2}$ versus $\varepsilon$ curve. c) Optical microscope image of h-BN flakes transferred onto $SiO_2$ substrate. d) Raman spectrum of h-BN film transferred onto $SiO_2$/Si substrate. The spectrum was background corrected by subtracting the background signal from $SiO_2$/Si substrate. e) Raman mapping of an h-BN flake near the edge. The arrow indicates the grain boundaries where a typical overlapping grain boundary can be found. Higher intensity of Raman signal is due to larger thickness. f) AFM image of h-BN flake transferred onto $SiO_2$/Si substrate. The inset shows the scan profile across the white arrow. The thickness is measured as ≈0.5 nm. g) SEM image of one such flake of Sample II transferred onto a copper grid coated with holey carbon film with the inset displaying a TEM image at the edge of the flake. h) SAED patterns at six different locations across the h-BN flake in (g) indicated by 1–6.

 © 2019 WILEY-VCH Verlag GmbH & Co. KGaA, Weinheim

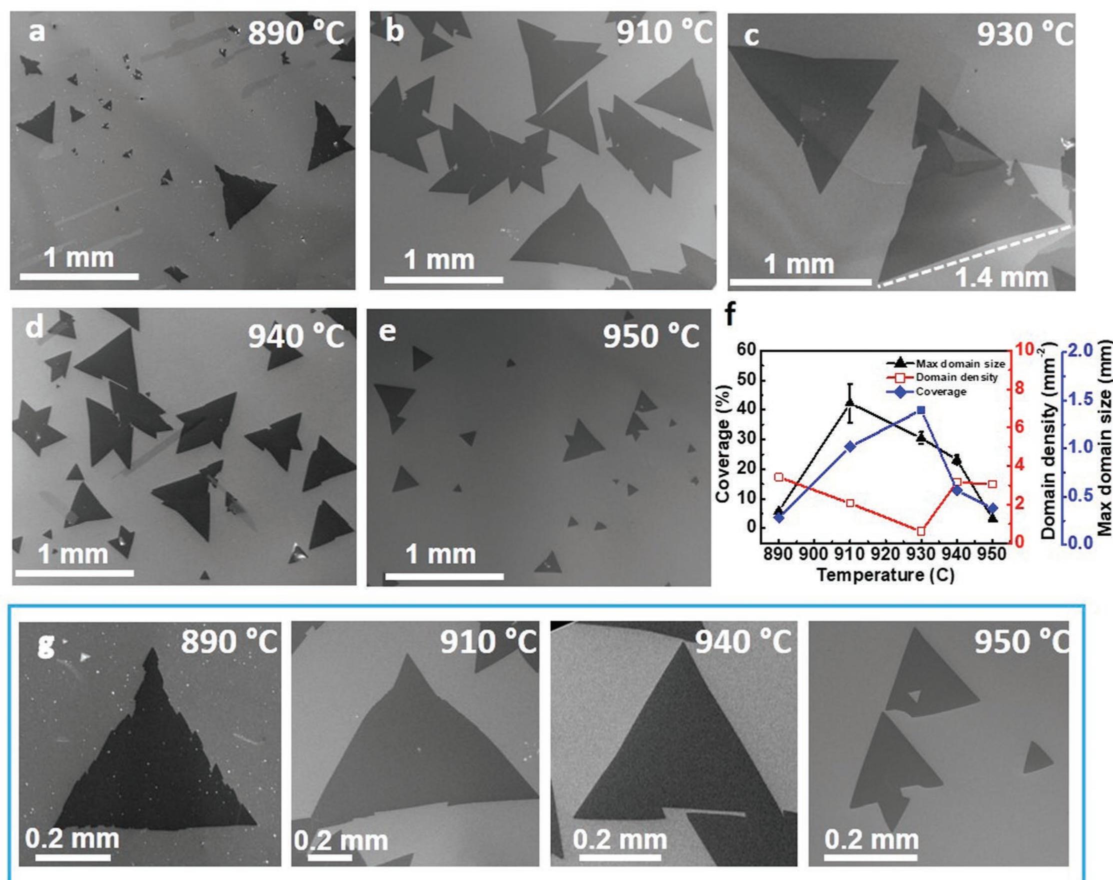


**Figure 5.** Substrate temperature control of large-size single-crystal h-BN flakes. a–e) SEM images of h-BN samples grown at 890, 910, 930, 940, and 950 °C, respectively. f) Plot of coverage, domain density, and maximum domain size as a function of temperature. g) Zoom-in SEM images showing typical h-BN flakes grown with different substrate temperature at 890, 910, 940, and 950 °C, respectively.

a full width at half maximum (FWHM) of 17.8 $cm^{-1}$, corresponding to monolayer h-BN[40] (Figure 4d). Large-area Raman mapping at the edge of a domain is presented in Figure 4e. The uniform contrast indicates good quality. It is worth noting that multilayer regions of finite width (≈5 µm) are often found at the grain boundaries. Similar phenomenon was reported and discussed elsewhere.[10] Figure 4f shows an atomic force microscopy (AFM) image of the transferred h-BN. A step height at the flake edge was measured as 0.5 nm, which is consistent with the monolayer h-BN thickness on $SiO_2$.[40] An AFM scan was also performed on the as-grown sample and the result is shown in Figure S2 (Supporting Information). The root-mean-square (RMS) roughness of the film is 3.67 nm while the RMS roughness of the AGG Ni substrate is ≈1.04 nm. The increased roughness is due to further reconstruction of the Ni surface during the growth of the h-BN film, which conforms onto the area.[38]

Transmission electron microscopy (TEM) analysis was conducted to confirm the single-crystal nature of the mm-sized h-BN domains. Figure 4g shows an SEM image of a mm-sized h-BN flake in Sample II which was transferred onto a mesh-200 Cu grid covered by holey carbon film. The h-BN flake outlined by blue dashed lines can be clearly seen, despite the residue introduced during the transfer process. SEM and OM images of the same flake on the as-grown sample area are also shown in the upper left and upper right insets, respectively. It is worth noting that the OM image was taken after oxidization in air in order to enhance the contrast. Selective area electron diffraction (SAED) patterns at six different spots were collected across the flakes as marked by the blue circles and labeled with numbers 1–6. The corresponding SAED patterns are shown in Figure 4h. The identical sixfold symmetric diffraction spots confirm the single crystallinity of the mm-sized domain and high quality. The monolayer layer nature is further confirmed by the TEM edge analysis (bottom left inset in Figure 4g).

Growth temperature plays an important role in the growth dynamics. **Figure 5**a–e shows SEM images of samples grown from 890 to 950 °C. All other growth conditions are the same including AGG Ni (100) substrate, 0.5 sccm acetlyne carburization for 5 min, amonnia source of 10 sccm, and boron cell at 1120 °C. Figure 5f shows a plot of the coverage, domain density, and maximum domain size as a function of the growth temperature. SEM images of typical h-BN domains obtained under different growth temperature are shown in Figure 5g. As seen from the SEM images, the domain shape changes from a concave triangle with dendritic edge to slightly convex triangle with straight edge as the substrate temperature increases. Similar results were achieved for the h-BN growth with mixed


© 2019 WILEY-VCH Verlag GmbH & Co. KGaA, Weinheim

nitrogen source as seen in Figure S3 (Supporting Information). In general, the growth of 2D material can be described by three sequential steps, that is, source atoms adsorption, adatoms hopping and diffusion across adsorption sites on substrate surface, and adatoms bonding and attachment to active sites of an existing domain edge. Each step has an associated energy barrier to overcome. Besides, the adatoms desorption and edge atoms detachment also happen at the same time. Adatom diffusion and attachment/detachment can directly affect the growth of a domain edge, and, therefore, can be typical limiting factors. In a diffusion-limited growth scenario, where the diffusion of adatoms is relatively slow with a high diffusion barrier, or the attachment is relatively effective, the 2D domain usually shows a concave shape with dendritic edges due to the variation in local concentration gradient of adatoms.[41] When the attachment energy barrier is increased and/or the diffusion barrier is decreased, the growth is then shifted to attachment/detachment limited growth. The domain shape often exhibits an equilibrium shape with straight edges according to the Wulf construction. The present temperature-dependent domain shape evolution results indicate the gradual transition from diffusion-limited growth mode to attachment/detachment-limited growth mode.

As seen from Figure 5f, the maximum domain size evolves with the growth temperature and the largest domain was achieved around 930 °C to be 1.4 mm (indicated in Figure 5c), which happens at the transition region between diffusion- and attachment/detachment-limited regions. This can be explained by the highest atomic efficiency. Further increase of the temperature leads to increased detachment/dissociation of the edge atoms, which limits the increase of the domain size. High desorption rate of B/N atoms also limits the supply of feedstock for edge attachment and limits the growth rate. The domain density remains in a low and similar level, and almost independent of temperature within a span of 60 °C (Figure 5f).

Precursor type and flux also have direct influence on the growth dynamics. Different N sources including pure $N_2$ plasma, pure $NH_3$, and their mixture contribute differently to the morphology of h-BN samples. Some results are shown in Figures 3 and 5 and Figure S3 (Supporting Information), and a comprehensive study of this aspect is reported elsewhere.[42] Likewise, the B flux is critical to the coverage of h-BN as well due to high desorption rate of B.[11,43] Therefore, changing $B_2O_3$ cell temperature will change the B flux, and, in turn, change the coverage and morphology of h-BN. As seen from Figure 3, the morphology changes from discrete h-BN flakes (Sample II) to continuous uniform h-BN monolayer film (Sample IV) after the $B_2O_3$ cell temperature increases from 1120 to 1130 °C. As the $B_2O_3$ cell temperature keeps increasing from 1130 to 1170 °C, besides the formation of continuous uniform h-BN monolayers, adlayers start to form and increase in density (Figure S4, Supporting Information). It has been reported that the hydrogen terminated graphene edge can facilitate the intercalation growth of graphene multilayers due to the weak edge-substrate coupling.[44] Because of the same intercalation mechanism, these adlayers are local h-BN multilayers rather than boron clusters or other forms of boron nitrides. Details about the formation and nature of these adlayers are reported elsewhere.[42]

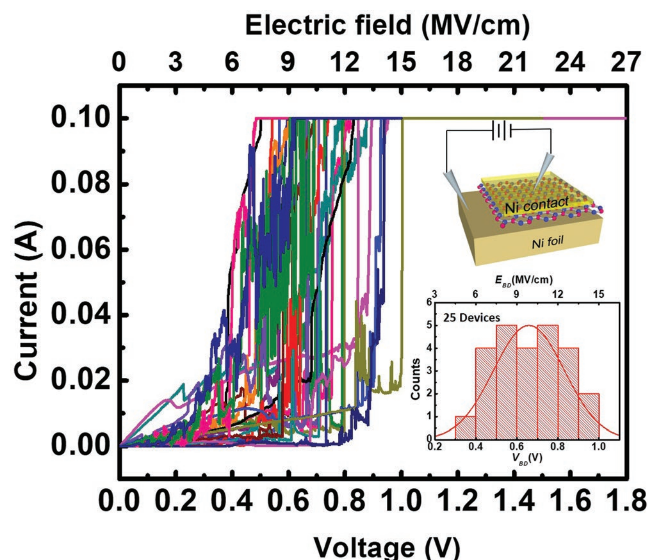


**Figure 6.** Electrical property of h-BN monolayer (Sample IV). Current–voltage characteristics of 25 Ni/h-BN/Ni capacitor devices. The upper and lower insets show the schematic of the device and the corresponding statistics of breakdown voltage ($V_{BD}$) and breakdown electric field ($E_{BD}$), respectively.

In order to study the quality of the as-grown continuous uniform h-BN monolayer, Ni(metal contact)/h-BN/Ni(foil) two-terminal devices with a metal contact size of $50 \times 50$ µm$^2$ based on Sample IV were fabricated (Experimental Section). **Figure 6** shows *I–V* characteristics of 25 devices, and the bottom right inset shows the distribution of corresponding breakdown voltages ($V_{BD}$). As seen from Figure 6, the devices operate under direct tunneling process at lower voltages and undergo typical soft breakdown as the bias increases to a certain voltage; the peak $V_{BD}$ is determined to be 0.65 V from a Gaussian fit. Assuming the interaction between the top/bottom Ni contacts with the middle single-layer h-BN is through Van der Waals forces, the Van der Waals distance between the top and bottom Ni contacts is ≈0.667 nm. Thus, the estimated average breakdown electric field is 9.75 MV cm$^{-1}$, which is slightly higher than the previous reported value of a three-layer h-BN film on Co and is comparable with that of exfoliated h-BN,[45] suggesting high quality of the single-layer h-BN film.

To reveal the epitaxial relationship between h-BN flakes and Ni (100) substrate, SEM imaging and EBSD analysis were combined to characterize the samples. Figure S6a,b (Supporting Information) shows SEM images of typical flakes at different locations of an h-BN sample. As seen from these images, most h-BN domains have one edge aligned along either [011] or [0$\bar{1}$1] directions. This is similar to the observation that h-BN flakes have two equivalent alignments on Cu (100) surface, being along two diagonal directions [011] and [0$\bar{1}$1], due to the four-fold symmetry of Cu (100).[46] In addition, the domains usually consist of one straight edge and two concave edges. This is reminiscent of the four-lobed graphene flakes grown on Cu (100).[47] We believe the anisotropic diffusion is also responsible for this phenomenon, as the concave edge is typical for diffusion-limited growth. Figure S6c (Supporting Information) shows a schematic of the formation of the asymmetric h-BN


© 2019 WILEY-VCH Verlag GmbH & Co. KGaA, Weinheim

a

| Adsorption Energy eV/atom | Adsorption sites | Ni (100) | |
|---|---|---|---|
| | | Pristine | With C |
| B | Top | 4.38 | 3.88 |
| | Hollow | 0.65 | 0.62 |
| | Bridge | 2.68 | 2.65 |
| N | Top | 7.69 | 0.639 |
| | Hollow | -2.75 | -2.80 |
| | Bridge | -1.13 | -1.18 |

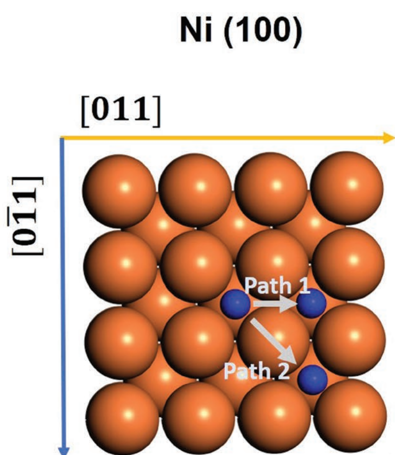


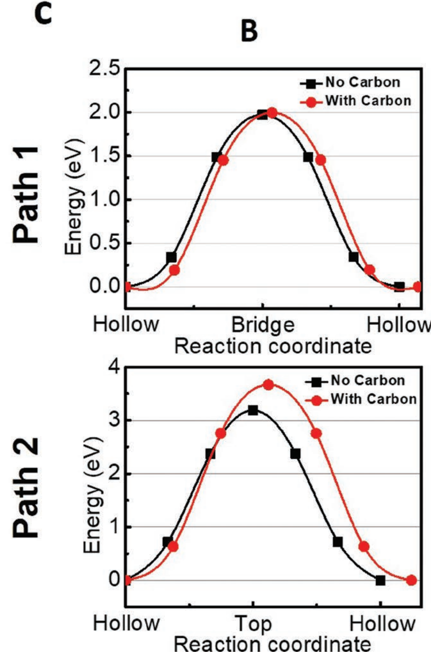


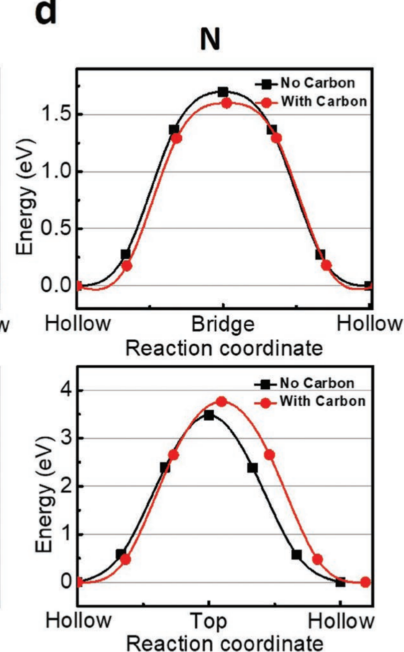


**Figure 7.** Theoretical calculation of adsorption and diffusion energies of B and N atoms on Ni (100). a) A summary of adsorption energies of B and N on Ni (100) with and without an embedded interstitial carbon. b–d) Reaction path from an NEB calculation showing the diffusion activation energy from one adsorption site to another. b) Top view of a Ni (100) surface with a B or N atom adsorbed on it. Two diffusion paths are indicated with white arrows. Minimum energy path along path 1 and path 2 for (c) a B and (d) an N atom diffusing from one hollow site to the neighboring hollow site of Ni (100) surface without (black curve) or with (red curve) interstitial carbon atom.

domains. The fast and slow diffusion directions are indicated by green and yellow arrows, respectively. With the given alignment configuration of Ni (100) substrate, the h-BN domains have one edge aligned with the [011] family direction. This straight edge is also perpendicular to a fast diffusion direction. On the other hand, the other two edges as two growth fronts are facing the slow diffusion direction. As a result, these edges are more prone to the depletion of local adatoms supply and fall into diffusion-limited region.

Finally, we briefly discuss the results from the thermodynamics point of view. As a matter of fact, the focal point of enabling the growth of large-area single-crystal h-BN here is the incorporation of carbon interstitials into secondary recrystalized Ni (100). Our earlier effort of the growth of h-BN on carburized Co (111) substrates has already indicated the enhanced adsorption and diffusion of B and N atoms on Co (111).[11] Since both Ni and Co are transition metals, this suggests that carbon incorporation into these substrates changes the catalytic effect of these metals. From the perspective of crystal growth, stronger catalytic effect is equivalent to smaller nucleation activation energy. The nucleation activation energy $E_a$ is expressed as[48,49]

$$E_a = E_{ads} + E_{diff} + E_{att} \quad (1)$$

namely, it is related to the adsorption energy $E_{ads}$, diffusion activation energy $E_{diff}$, and nucleation barrier or energy barrier of

 © 2019 WILEY-VCH Verlag GmbH & Co. KGaA, Weinheim

attachment for the capture of a surface adatom by a supercritical nucleus $E_{att}$. As seen from Equation (1), at a given temperature and source flux, the increase of adsorption, diffusion, and attachment, namely, smaller adsorption energy ($E_{ads}$), diffusion energy ($E_{diff}$), and attachment energy ($E_{att}$) can promote the nucleation of h-BN. Since the attachment energy is an energy barrier for a B or N atom to overcome to attach covalently to an existing nuclei on the substrate, the attachment energies will be the same for a given transition metal with or without interstitials if the change of the lattice parameters of a metal substrate is assumed to be negligible after the incorporation of small and moderate amount of interstitials. Therefore, an understanding of the change of adsorption energy and diffusion energy before and after the incorporation of carbon interstitial can help understand the h-BN nucleation and growth on Ni here.

The adsorption energies of B and N atoms on Ni are calculated using the following expression

$$E_{ads} = E_{B/N\ on\ surface} - E_{B/N} - E_{surface} \quad (2)$$

where $E_{B/N\ on\ surface}$ is the total energy of a B or N atom on the surface of a supercell. $E_{B/N}$ is the chemical potential of the adsorbed B or N atom, and $E_{surface}$ is the total energy of the isolated supercell. Detailed methodology of the DFT simulation of adsorption energy is in the Experimental Section. **Figure 7**a shows a summary of adsorption energies of B and N atoms onto top, hollow, and bridge sites of Ni (100) with and without embedded carbon interstitials. As seen from Figure 7a, the adsorption energies of B and N atoms decrease on Ni (100) after the incorporation of carbon interstitials. As a result, the activation energy reduces for carburized Ni (100).

To study the carbon interstitial effect on diffusion activation energy ($E_{diff}$) of B and N atoms, simulations using the climbing image nudged elastic band (CI-NEB) method were carried out (Experimental Section). For Ni (100) substrate (Figure 7b), Figure 7c,d shows the diffusion energies for both B and N atoms along two directions from one hollow site to another, denoted as path 1 and path 2 in Figure 7b. The diffusion barriers for both B and N along path 2 are larger than that along path 1 with or without carbon in the substrate, which confirms the hypothesis of the fast and slow diffusion directions to be path 1 and path 2, respectively. After the incorporation of carbon, the diffusion energies for B and N along path 2 are further increased while that along path 1 are almost unchanged and decreased, respectively. This suggests that although the nucleation may still take the slow diffusion path 2, it dominantly takes the fast diffusion path (path 1). Overall, the unchanged B and reduced N diffusion energies along path 1 and reduced B and N adsorption energies contribute to the reduction of nucleation activation energy, in turn, the nucleation and growth of h-BN become more efficient, leading to larger single-crystal h-BN flakes and eventually continuous high-quality monolayer films on carburized Ni (100). Finally, it should be noted that the calculated values of absorption and diffusion energies may not be absolute to represent real thermodynamic situation precisely due to relative simplification in the above simulations, such as using small supercell, considering individual atoms rather than group of atoms and their interactions, etc. However, the change of these values can reasonably explain different nucleation and growth of h-BN on Ni (100) with and without carburization.

## 3. Conclusion

In conclusion, we demonstrated controllable synthesis of millimeter-size single-crystal h-BN domains through an interstitial carbon assisted approach. Interstitial C atoms in Ni (100) substrates promote B and N adsorption and push the growth into fast diffusion regions, which essentially reduces nucleation activation energy. With proper preparation of high-quality substrates, which yields large Ni (100) grains, single-crystal h-BN monolayer domains over 1 mm were routinely obtained and a large single-crystal h-BN domain of 1.4 mm was achieved. Continuous large-area single-layer h-BN film with a high breakdown electric field of 9.75 MV $cm^{-1}$ was also demonstrated. The growth dynamics were studied by tuning different growth parameters including substrate temperature, and B and N source fluxes. The epitaxial relationship between h-BN and substrate was studied with the assistance of EBSD mapping. The in-depth experimental analysis combined with the support of DFT simulations paves the way towards full understanding of the growth mechanism of 2D h-BN on transition metal substrates. The experimental demonstration of millimeter-sized large single-crystal h-BN domains and continuous large-area single-layer h-BN films represents a further step toward practical applications of these 2D materials.

## 4. Experimental Section

*Substrate Preparation*: Ni foils with a thickness of 0.1 mm and a purity of 99.995% from Alfa Aesar were polished on a SBT 920 Lapping and Polishing workstation and cut into 1 cm × 1 cm pieces as substrates. These pieces were degreased and deoxidized with acetone, IPA, and diluted hydrochloric acid (10%), rinsed in deionized (DI) water, blown dry and finally loaded into an MBE chamber.

*Hydrogen Annealing and Carburization*: A re-designed Perkin-Elmer MBE system with a background pressure of $\approx 10^{-9}$ Torr was used for the sample growth. The substrate was heated to 950 °C and annealed at this temperature under a 10 sccm flow of hydrogen gas for 60 min to enhance the recrystallization of Ni. Then, the substrate temperature was adjusted to the growth temperature. 0.5 sccm $C_2H_2$ gas was introduced into chamber with a pressure of $5 \times 10^{-5}$ Torr to enrich Ni with carbon prior to h-BN growth. H-BN growth step started after the carburization process.

*h-BN Growth*: A Knudsen effusion cell filled with $B_2O_3$ powder (Alfa Aesar, 99.999% purity) was used as boron (B) source. Nitrogen plasma (Airgas, 99.9999% purity) generated by an electron cyclotron resonance (ECR) system and high-purity ammonia (American Gas Group, 99.9995% purity) were used as nitrogen (N) sources. The h-BN growth was conducted by simultaneous introduction of B and N sources onto the Ni substrate at 890–950 °C. B cell temperature was maintained at constant temperature throughout the growth. $NH_3$ gas was controlled at a constant flow rate by a mass flow controller (MFC) and introduced to the chamber through a shut-off valve. Nitrogen plasma as an alternative N source is generated from an ECR plasma source with a power of 228 W. The growth pressure was on the order of $10^{-4}$ Torr. After the growth, the samples were cooled to room temperature at a rate of 10 °C $min^{-1}$.

*Transferring of h-BN Samples*: The Ni substrates were etched by $FeCl_3$/HCl solution after spin-coating PMMA (495 A4) on as-grown samples. The PMMA/h-BN stack was then transferred into 10% HCl, 5% HCl, and DI water successively to rinse out the residual etchant. The floating h-BN film was taken out by a desired substrate and left to dry for at least 12 h. After that, a few drops of PMMA were deposited again on the transferred film and soaked for another 2 h. The additional PMMA was used to soften the previous PMMA layer and enhance the attachment


© 2019 WILEY-VCH Verlag GmbH & Co. KGaA, Weinheim

of h-BN on the substrate. PMMA was removed by dipping the sample into acetone bath. Finally, the sample was annealed at 400 °C inside a CVD furnace for 3 h in $Ar/O_2$ flow of 300 sccm to remove any remaining organic residue.

*Characterizations*: SEM images were acquired using an FEI NNS450 system in secondary electron (SE) imaging mode with a beam voltage of 10 kV. Raman characterizations were performed using a HORIBA LabRam system equipped with a 60 mW, 532 nm green laser. XPS characterization was conducted using a Kratos AXIS ULTRA XPS system equipped with an Al K$\alpha$ monochromatic X-ray source and a 165 mm mean radius electron energy hemispherical analyzer. The fitting of XPS data was performed using CasaXPS software. As-measured XPS data were first calibrated by using Ni $2p_{3/2}$ peak at 852.6 eV (Lorentzian Asymmetric line shape). B 1s and N 1s peaks were convoluted with Gaussian/Lorentzian line shape after background-corrected by Shirley type background. AFM images were obtained using a Veeco D5000 AFM system. TEM images and SAED patterns were acquired using a FEI Tecnai12 system. TEM sample was prepared by picking a transferred h-BN film using a 200-mesh Cu grid covered with holey carbon film with orthogonal array of 1.2 µm diameter holes.

*Device Fabrication and Electrical Measurement*: Ni(contact)/h-BN/Ni(foil) two-terminal devices were fabricated by a standard photolithography and lift-off process. A Ni layer of 100 nm was patterned as top square contacts with an edge length of 50 µm on the surface of as-grown h-BN film. Reactive ion etching (RIE) was performed with a 50 sccm $SF_6$ plasma, under a power of 50 W, and for 15 s to etch the h-BN film between devices, which ensured isolation of different devices on the same substrate. Current–voltage ($I$–$V$) characteristics were obtained by an Agilent 4155C semiconductor parameter analyzer equipped with probing tips having a diameter of about 5 µm (Signatone, SE-TL).

*DFT Calculations*: First-principles DFT calculations used the projector augmented wave method and the Perdew–Burke–Ernzerhof (PBE) type generalized gradient approximation[50,51] as implemented in the software package VASP.[52] Spin polarization was included self-consistently in all calculations. For the unit cell calculations, a Monkhorst–Pack scheme was adopted to integrate over the Brillouin zone with a k-mesh of 9 × 9 × 1. A plane-wave basis cutoff of 550 eV was used. All structures were optimized until the largest force on the atoms was less than 0.01 eV $Å^{-1}$. The adsorption energies of B and N atoms on the (100) surface of Ni were modeled. A single B or N atom was placed on specific sites of the surface of a supercell consisting of four atomic layers of Ni atoms. The supercell size in the *XY*-plane for (100) surface is 4 × 4. The integration over the Brillouin zone for the surfaces was done with a converged k-mesh of 3 × 3 × 1. These sites include the top, twofold bridge, and fourfold hollow site of Ni (100), on which the adsorption of B or N atoms would enable an epitaxial relationship between h-BN and the substrates. A vacuum gap of 15 Å was introduced to avoid interactions between the periodically repeated surfaces. To simulate the diffusion activation energies, the CI-NEB method was adopted.[53] The spring force between adjacent images was set to 5.0 eV $Å^{-1}$. The migration energies, namely, diffusion activation energies were obtained for the different adsorbates between the different sites of the (100) surface of Ni. The initial and final positions of the adsorbed atoms were set at two hollow sites of Ni (100). Eight images were considered to calculate the activation energies between the initial and final states. For calculation of adsorption and diffusion energies for B and N on carbon-incorporated Ni, one interstitial carbon occupying the octahedral site in a supercell of Ni (100), which is 1.58 Å below the surface, was assumed.

## Supporting Information

Supporting Information is available from the Wiley Online Library or from the author.

## Acknowledgements

The authors acknowledge the support by FAME, one of six centers of STARnet, a Semiconductor Research Corporation program supported by MARCO and DARPA. This work was supported in part by SHINES, an Energy Frontier Research Center funded by the U.S. Department of Energy, Office of Science, Basic Energy Sciences under Award No. SC0012670. J.L. led the project. H.T. designed and performed the experimental works. P.D. and R.L. carried out the DFT calculations. Y.H. contributed to sample transferring and AFM measurement. Z.C. contributed to electrical measurement and analysis. W.S. performed absorption measurement. H.T. and J.L. wrote the manuscript. All authors contributed to analyzing and reviewing the data in this manuscript and commented on the manuscript.

## Conflict of Interest

The authors declare no conflict of interest.

## Keywords

2D, breakdown electric field, catalytic effect, domain size, hexagonal boron nitride (h-BN), interstitial carbon, molecular beam epitaxy (MBE), single crystal

Received: July 11, 2019
Revised: September 6, 2019
Published online:

[1] L. Song, L. Ci, H. Lu, P. B. Sorokin, C. Jin, J. Ni, A. G. Kvashnin, D. G. Kvashnin, J. Lou, B. I. Yakobson, *Nano Lett.* **2010**, *10*, 3209.
[2] K. K. Kim, A. Hsu, X. Jia, S. M. Kim, Y. Shi, M. Hofmann, D. Nezich, J. F. Rodriguez-Nieva, M. Dresselhaus, T. Palacios, *Nano Lett.* **2012**, *12*, 161.
[3] M. Xu, T. Liang, M. Shi, *Chem. Rev.* **2013**, *113*, 3766.
[4] J. Yin, J. Li, Y. Hang, J. Yu, G. Tai, X. Li, Z. Zhang, W. Guo, *Small* **2016**, *12*, 2942.
[5] Y. Hao, M. Bharathi, L. Wang, Y. Liu, H. Chen, S. Nie, X. Wang, H. Chou, C. Tan, B. Fallahazad, *Science* **2013**, *342*, 720.
[6] Y. Gong, G. Ye, S. Lei, G. Shi, Y. He, J. Lin, X. Zhang, R. Vajtai, S. T. Pantelides, W. Zhou, *Adv. Funct. Mater.* **2016**, *26*, 2009.
[7] T. Wu, X. Zhang, Q. Yuan, J. Xue, G. Lu, Z. Liu, H. Wang, H. Wang, F. Ding, Q. Yu, *Nat. Mater.* **2016**, *15*, 43.
[8] X. Xu, Z. Zhang, J. Dong, D. Yi, J. Niu, M. Wu, L. Lin, R. Yin, M. Li, J. Zhou, *Sci. Bull.* **2017**, *62*, 1074.
[9] J. Meng, X. Zhang, Y. Wang, Z. Yin, H. Liu, J. Xia, H. Wang, J. You, P. Jin, D. Wang, *Small* **2017**, *13*, 1604179.
[10] H. Tian, A. Khanaki, P. Das, R. Zheng, Z. Cui, Y. He, W. Shi, Z. Xu, R. Lake, J. Liu, *Nano Lett.* **2018**, *18*, 3352.
[11] J. S. Lee, S. H. Choi, S. J. Yun, Y. I. Kim, S. Boandoh, J.-H. Park, B. G. Shin, H. Ko, S. H. Lee, Y.-M. Kim, *Science* **2018**, *362*, 817.
[12] H. Cun, A. Hemmi, E. Miniussi, C. Bernard, B. Probst, K. Liu, D. T. Alexander, A. Kleibert, G. Mette, M. Weinl, *Nano Lett.* **2018**, *18*, 1205.
[13] L. Wang, X. Xu, L. Zhang, R. Qiao, M. Wu, Z. Wang, S. Zhang, J. Liang, Z. Zhang, Z. Zhang, *Nature* **2019**, *570*, 91.
[14] R. Y. Tay, H. J. Park, G. H. Ryu, D. Tan, S. H. Tsang, H. Li, W. Liu, E. H. T. Teo, Z. Lee, Y. Lifshitz, *Nanoscale* **2016**, *8*, 2434.
[15] M. S. Driver, J. D. Beatty, O. Olanipekun, K. Reid, A. Rath, P. M. Voyles, J. A. Kelber, *Langmuir* **2016**, *32*, 2601.

 © 2019 WILEY-VCH Verlag GmbH & Co. KGaA, Weinheim

[16] Z. Xu, H. Tian, A. Khanaki, R. Zheng, M. Suja, J. Liu, *Sci. Rep.* **2017**, *7*, 43100.
[17] Y. Shi, C. Hamsen, X. Jia, K. K. Kim, A. Reina, M. Hofmann, A. L. Hsu, K. Zhang, H. Li, Z.-Y. Juang, *Nano Lett.* **2010**, *10*, 4134.
[18] A. Ismach, H. Chou, D. A. Ferrer, Y. Wu, S. McDonnell, H. C. Floresca, A. Covacevich, C. Pope, R. Piner, M. J. Kim, *ACS Nano* **2012**, *6*, 6378.
[19] S. Caneva, R. S. Weatherup, B. C. Bayer, B. Brennan, S. J. Spencer, K. Mingard, A. Cabrero-Vilatela, C. Baehtz, A. J. Pollard, S. Hofmann, *Nano Lett.* **2015**, *15*, 1867.
[20] S. M. Kim, A. Hsu, M. H. Park, S. H. Chae, S. J. Yun, J. S. Lee, D.-H. Cho, W. Fang, C. Lee, T. Palacios, *Nat. Commun.* **2015**, *6*, 8662.
[21] S. Caneva, R. S. Weatherup, B. C. Bayer, R. Blume, A. Cabrero-Vilatela, P. Braeuninger-Weimer, M.-B. Martin, R. Wang, C. Baehtz, R. Schloegl, *Nano Lett.* **2016**, *16*, 1250.
[22] R.-J. Chang, X. Wang, S. Wang, Y. Sheng, B. Porter, H. Bhaskaran, J. H. Warner, *Chem. Mater.* **2017**, *29*, 6252.
[23] Y.-J. Cho, A. Summerfield, A. Davies, T. S. Cheng, E. F. Smith, C. J. Mellor, A. N. Khlobystov, C. T. Foxon, L. Eaves, P. H. Beton, *Sci. Rep.* **2016**, *6*, 34474.
[24] A. Summerfield, A. Davies, T. S. Cheng, V. V. Korolkov, Y. Cho, C. J. Mellor, C. T. Foxon, A. N. Khlobystov, K. Watanabe, T. Taniguchi, *Sci. Rep.* **2016**, *6*, 22440.
[25] S. Nakhaie, J. Wofford, T. Schumann, U. Jahn, M. Ramsteiner, M. Hanke, J. Lopes, H. Riechert, *Appl. Phys. Lett.* **2015**, *106*, 213108.
[26] Z. Xu, A. Khanaki, H. Tian, R. Zheng, M. Suja, J.-G. Zheng, J. Liu, *Appl. Phys. Lett.* **2016**, *109*, 043110.
[27] Z. Xu, R. Zheng, A. Khanaki, Z. Zuo, J. Liu, *Appl. Phys. Lett.* **2015**, *107*, 213103.
[28] R. Zheng, A. Khanaki, H. Tian, Y. He, Y. Cui, Z. Xu, J. Liu, *Appl. Phys. Lett.* **2017**, *111*, 011903.
[29] A. Khanaki, H. Tian, Z. Xu, R. Zheng, Y. He, Z. Cui, J. Yang, J. Liu, *Nanotechnology* **2018**, *29*, 035602.
[30] T. Kusama, T. Omori, T. Saito, S. Kise, T. Tanaka, Y. Araki, R. Kainuma, *Nat. Commun.* **2017**, *8*, 354.
[31] E. Zielinski, R. Vinci, J. Bravman, *J. Appl. Phys.* **1994**, *76*, 4516.
[32] T. Omori, T. Kusama, S. Kawata, I. Ohnuma, Y. Sutou, Y. Araki, K. Ishida, R. Kainuma, *Science* **2013**, *341*, 1500.
[33] R. Wang, D. G. Purdie, Y. Fan, F. C. Massabuau, P. Braeuninger-Weimer, O. J. Burton, R. Blume, R. Schloegl, A. Lombardo, R. S. Weatherup, *ACS Nano* **2019**, *13*, 2114.
[34] S. Nakhaie, M. Heilmann, T. Krause, M. Hanke, J. M. J. Lopes, *J. Appl. Phys.* **2019**, *125*, 115301.
[35] A. Tonkikh, E. Voloshina, P. Werner, H. Blumtritt, B. Senkovskiy, G. Güntherodt, S. Parkin, Y. S. Dedkov, *Sci. Rep.* **2016**, *6*, 23547.
[36] D. Chrysostomou, J. Flowers, F. Zaera, *Surf. Sci.* **1999**, *439*, 34.
[37] X. Kong, H. Ji, R. D. Piner, H. Li, C. W. Magnuson, C. Tan, A. Ismach, H. Chou, R. S. Ruoff, *Appl. Phys. Lett.* **2013**, *103*, 043119.
[38] N. R. Wilson, A. J. Marsden, M. Saghir, C. J. Bromley, R. Schaub, G. Costantini, T. W. White, C. Partridge, A. Barinov, P. Dudin, *Nano Res.* **2013**, *6*, 99.
[39] C. Elias, P. Valvin, T. Pelini, A. Summerfield, C. Mellor, T. Cheng, L. Eaves, C. Foxon, P. Beton, S. Novikov, *Nat. Commun.* **2019**, *10*, 2639.
[40] J. Han, J.-Y. Lee, H. Kwon, J.-S. Yeo, *Nanotechnology* **2014**, *25*, 145604.
[41] J. Dong, L. Zhang, F. Ding, *Adv. Mater.* **2019**, *31*, 1801583.
[42] Y. He, H. Tian, A. Khanaki, W. Shi, J. Tran, Z. Cui, P. Wei, J. Liu, *Appl. Surf. Sci.* **2019**, *498*, 143851.
[43] J. A. Rodriguez, C. M. Truong, J. S. Corneille, D. W. Goodman, *J. Phys. Chem.* **1992**, *96*, 334.
[44] H. Shu, X. Chen, F. Ding, *Chem. Sci.* **2014**, *5*, 4639.
[45] Y. Hattori, T. Taniguchi, K. Watanabe, K. Nagashio, *ACS Nano* **2015**, *9*, 916.
[46] G. E. Wood, A. J. Marsden, J. J. Mudd, M. Walker, M. Asensio, J. Avila, K. Chen, G. R. Bell, N. R. Wilson, *2D Mater.* **2015**, *2*, 025003.
[47] D. H. Jung, C. Kang, J. E. Nam, H. Jeong, J. S. Lee, *Sci. Rep.* **2016**, *6*, 21136.
[48] T. Li, C. Liu, Z. Zhang, B. Yu, H. Dong, W. Jia, Z. Jia, C. Yu, L. Gan, B. Xu, *Nanoscale Res. Lett.* **2018**, *13*, 130.
[49] R. Yue, Y. Nie, L. A. Walsh, R. Addou, C. Liang, N. Lu, A. T. Barton, H. Zhu, Z. Che, D. Barrera, *2D Mater.* **2017**, *4*, 045019.
[50] J. P. Perdew, K. Burke, M. Ernzerhof, *Phys. Rev. Lett.* **1996**, *77*, 3865.
[51] M. Ernzerhof, G. E. Scuseria, *J. Chem. Phys.* **1999**, *110*, 5029.
[52] G. Kresse, J. Hafner, *Phys. Rev. B* **1993**, *47*, 558.
[53] G. Henkelman, B. P. Uberuaga, H. Jónsson, *J. Chem. Phys.* **2000**, *113*, 9901.


© 2019 WILEY-VCH Verlag GmbH & Co. KGaA, Weinheim